



A Graphical User Interface for Proton Beam Monitoring

MPhys Project Semester Two Report

Lewis Dean
Student ID: 10823674

Performed in collaboration with Robin de Freitas (10887826)

Supervisors: Prof. Cinzia Da Via and Prof. Stephen Watts

University of Manchester
Department of Physics and Astronomy
June 5, 2025

Abstract

A Graphical User Interface, coined CRISP, has been developed for imaging scintillation light emitted by proton interactions within plastic scintillators. The interface features tools for camera calibrations, enabling the live analysis of scintillation light images at a proton beamline if said calibrations are performed in advance. The software was tested in a visit to The Christie Hospital's Proton Beam Therapy Centre in April; the results of those experiments are summarised in this report. Monte-Carlo simulations were conducted to assess the accuracy of Bragg peak depths determined by CRISP's analysis. Unfortunately, comparisons between simulated and experimental Bragg peak depths were limited by the precision of our simulations.

1 Introduction

The study of proton beam dynamics is of particular importance to Proton Beam Therapy (PBT), a radiotherapy for cancer treatment initially proposed by Robert Wilson in 1946 [1]. Unlike photon radiotherapy, during which photons interact with healthy tissue both proximal and distal to the tumour, PBT allows the more precise delivery of dose baths to tumours [2]. This is because heavy charged particles, like protons, deposit most of their energy around a portion of their trajectories known as the Bragg peak. The depth of this region can be tuned through the beam's energy, so that a tumour's absorbed dose is then set through the proton beam's current. Additionally, an appropriate superposition of proton energies determined by treatment plan algorithms produces a spread-out-Bragg-peak (SOBP), allowing the dose to conform to the tumour shape along the beam's axis. These same algorithms inform how the beam should be scanned across a patient to conform the dose with a tumour's lateral distribution.

This precision in dose delivery makes PBT an excellent candidate for non-invasive cancer treatment, however the equipment involved makes this an expensive method compared to photon radiotherapy. One of two clinical proton beams in the UK is at The Christie Hospital's Proton Beam Therapy Centre. To produce their beam, protons are generated through the electrolysis of water, after which they are accelerated to therapeutic energies using a cyclotron. The Lorentz force imparted by the cyclotron to these protons consists of a centripetal force, arising from a magnetic field perpendicular to the proton orbits, and a tangential electric force that accelerates the protons to approximately $0.6c$ [3]. At this speed, a proton beam is extracted from the cyclotron using magnets, after which the beam is attenuated to the desired clinical energy with an Energy Selection System (ESS).

Spanning a year-long project, my lab partner, Robin de Freitas, and I have developed a Graphical User Interface (GUI) for a proton beam monitoring system. Building upon an experimental setup designed the previous year, scintillation light is imaged, generated during proton beam interactions with a plastic scintillator, using the cameras of Raspberry Pi computers. Our GUI allows for the calibration of these cameras, the optimal imaging of scintillation light, and the analysis of light distributions to calculate Bragg peak depths within the scintillator. Given this range of functionality, we have named our software with the acronym CRISP: Calibration and Research Imaging System for Plastic scintillators. This report outlines how users would interact with our software, and provides a discussion of experiments performed through CRISP at The Christie Proton Beam Therapy Centre in April.

2 Experimental Apparatus

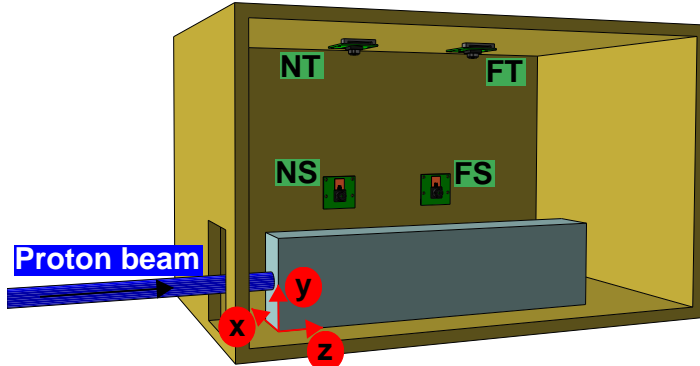


Figure 1: A schematic of the wooden box used in our experiments to house the scintillator and Raspberry Pi cameras. The camera labels (NS, FS, NT, FT) correspond to both a camera's mounted position and how close it is to the beam's entrance point. The box's coordinate system is depicted by the red axes. This diagram was created by my project partner, Robin de Freitas.

Within Figure 1, a schematic is given of the wooden box used to house our apparatus. A proton beam is able to enter the box through a rectangular hole, after which it will be incident upon the anterior face of a plastic scintillator. Note the dimensions of this scintillator are given in Table 1. The plastic's long-chain polymers have many more vibrational states than they do electronic. This means that excited atomic electrons are unlikely to de-excite to their original electronic energy levels, but rather to vibrational excitations of them. Thus, the energy of photons emitted by de-excitation is often insufficient to excite further electrons, and they go on to escape the scintillator.

Table 1: Dimensions of the plastic scintillator used in our experiment.

Axis	Dimension [mm]
x	38.8 ± 0.1
y	99.8 ± 0.1
z	249.5 ± 0.5

This describes the production of scintillation light, to be imaged by the four cameras mounted inside the box. They have been labelled NS, FS, NT and FT - the first letter reflects the camera's proximity to the beam entrance (N for near, F for far) and the second letter signifies where the camera is mounted (S for side-mounted, T for top-mounted). The camera model used is Arducam's 16MP IMX519 [4], and each is controlled through their own Raspberry Pi computer, mounted to the box's exterior. A router is needed to connect the series of Pis to a CRISP user's local device over Ethernet. In addition to providing camera mounting points, the box shields the camera from external light that could otherwise interfere with scintillation light imaging. Unlike the Figure 1 schematic, the real box has its interior painted black to minimise scintillation light reflection.

A crucial detail of Figure 1 is the origin's position within the coordinate system we have defined for the box, namely on the bottom right corner of the anterior scintillator face. The x , y and z axis orientations are also labelled. This convention should be followed by all future users of CRISP (even with new box setups) to ensure the calibration process works as intended. Wooden blocks are mounted to the base of the box such that the scintillator always returns to the same place, ensuring the origin's position is invariant.

The scintillation light we image refracts as it exits the scintillator. In order to accurately locate events inside the scintillator, refraction needs accounting for, which requires its refractive index. Unfortunately, as was the case last semester, we are unaware of the exact plastic the scintillator is made from. A density measurement of $1.04 \pm 0.03 \text{ g cm}^{-3}$ implies it is likely polyvinyltoluene (PVT) [5]. However, PVT is dispersive and, since the primary fluor used when making the scintillator is unknown (emission wavelength unknown), the refractive index is indeterminate. Performing refraction measurements ourselves would not be useful unless we used a laser of the same wavelength as our scintillator emits. Therefore, we have resorted to assuming a refractive index of 1.66, identified in Nakamura et Al [6] as an effective refractive index for PVT scintillators.

The images of our real setup in Section 7 show extra equipment around the exterior of the box, e.g. a silver railing. These features were added to facilitate experiments conducted by Professor Stephen Watts and PhD student Mosst Tasnim Binte Shawkat.

3 Proton Beam Physics

Within proton beam therapy, the effective dose delivered to a patient's tissue is proportional to the absorbed dose D , up to a factor parameterising the tissue's radiosensitivity. For a proton beam traversing a plastic scintillator, the scintillation light intensity emitted from a given cross-section is proportional to that cross-section's absorbed dose. If the protons constituting the beam have instantaneous energy E_p , the absorbed dose in a cross-section of the material is calculated with the following equation [7]:

$$D = \Phi \frac{S}{\rho}. \quad (1)$$

Φ is the fluence of the proton beam, i.e. how many protons there are per unit area normal to the beam axis. The factor $\frac{S}{\rho}$ is known as the mass stopping power, wherein ρ is the material's mass density and S is the stopping power, defined as,

$$S = -\frac{dE_p}{dx}, \quad (2)$$

$$\frac{dE_p}{dx} = \text{LET}, \quad (3)$$

where x is the depth traversed through the medium. The derivative of proton energy with respect to depth has been coined the “linear energy transfer” (LET), and it can be calculated for heavy charged particles like protons using the Bethe-Bloch (B-B) equation. When deriving the B-B equation, proton energy loss within the medium is modelled through atomic electron interactions, rather than nuclear interactions, and E_p is assumed much greater than the binding energy of atomic electrons such that the electrons can be approximated as at rest. Furthermore, one assumes only a small fraction of E_p is lost per electronic interaction, an assumption known as the Continuous-Slowing-Down Approximation (CSDA). For the therapeutic energies used in our experiment (70 MeV to 170 MeV), the non-relativistic B-B equation reflects the stopping power accurately; a key proportionality to understanding non-relativistic B-B dynamics is the fact that,

$$-\frac{dE_p}{dx} \propto \frac{1}{v^2}, \quad (4)$$

where v is the velocity of the proton. From this, one can see that protons lose their energy at an increasing rate as they slow. Consequently, the distribution of absorbed dose within the material, known as the Bragg curve, is sharply peaked towards the end of the proton trajectory, within a region known as the Bragg peak. An example Bragg curve is given in Figure 2. Despite the proportionality in Equation 4, the Bragg peak occurs at non-zero velocity (non-zero kinetic energy) since the material’s mean ionisation energy eventually prevents further proton-electron interactions. For an ensemble of protons within a beam, the dose’s Bragg peak has finite width due to a phenomenon called range-straggling; that is, the proton-electron interactions are ultimately statistical and thus two protons can actually peak in LET at slightly different depths. The Bragg peak width also grows with uncertainty in the nominal beam energy, E_B . An approximation for modelling Bragg curves is the Bortfeld function, derived by Thomas Bortfeld in 1996 [8], and we fit “Bortfelds” to beam-axis scintillation light distributions during our image analysis.

Another quantity for representing a proton beam’s penetration depth is the mean range. This is the depth beyond the Bragg peak in which the absorbed dose falls to half of that at the Bragg peak. Our analysis allows for the calculation of both Bragg peak depths and mean ranges.

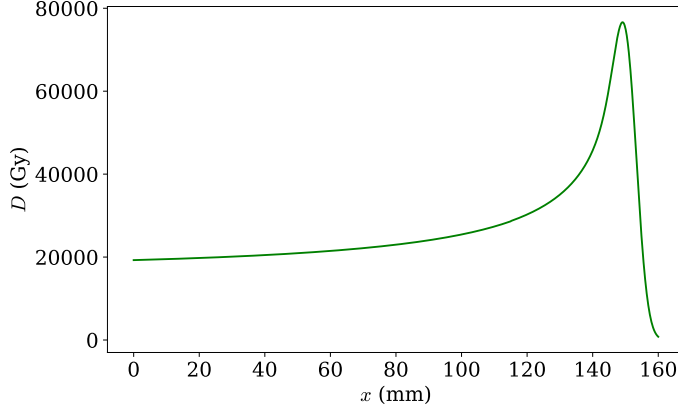


Figure 2: An example Bortfeld function which approximates the Bragg curve of absorbed dose with penetration depth.

The dose distribution transverse to the beam-axis is governed by the multi-Coulomb scattering (MCS) of protons from nuclei. Rutherford demonstrated that the differential cross-section for a projectile’s Coulomb scattering is proportional to $\frac{1}{\theta^4}$, where θ is the scattering angle. This clearly favours small θ , and hence small, independent and identically distributed (assuming CSDA) scatters accumulate as the protons propagate. This allows the central limit theorem to be invoked, and we expect the transverse dose distribution to be largely Gaussian. Since protons have the potential to have been scattered further from the beam-axis the deeper they have traversed into the material, the beam broadens with depth. That being said, the assumption of small, soft scatters breaks down around the Bragg peak. The low energy of the protons means the CSDA breaks down, and the probability of nuclear interactions, with larger scattering angles, increases [7]. In addition to this, for our experimental setup, protons often reach depths beyond the beam’s focus. Both of these considerations exacerbate beam broadening. Therefore, when fitting to the transverse scintillation light in our images, a generalised Gaussian model is used, taking the following form:

$$I(x) = A \exp \left[-\left(\frac{1}{2} \left(\frac{x-\mu}{\sigma} \right)^2 \right)^n \right] + I_0. \quad (5)$$

A is a normalisation constant, μ the Gaussian centre, σ the standard deviation, and I_0 a constant accounting for background light intensity. The shape parameter n is constrained to $n \geq 1$, allowing only the broadening of the Gaussian peak. For conciseness, this model is often referred to simply as a Gaussian.

4 Camera Calibration Theory

A method for 3D pinpointing events within images was devised last semester through the use of plane-to-plane homographies [9], [10]. To summarise, homographies are used in computer vision to map an event from a pixel (its image coordinate) onto some associated world plane (a physical spatial position). That is,

$$\mathbf{X} = \mathcal{H}\mathbf{x}, \quad (6)$$

where \mathbf{X} is a homogenous position vector on the world plane, \mathbf{x} is that on the image plane, and \mathcal{H} is the homography matrix. To calibrate a given world plane for a camera, first we print a checker board pattern and tape it to a rigid board to ensure its planarity. We then image that pattern placed at the desired world plane and use the computer vision library OpenCV to identify which pixels contain the checker board's corners, $\{\mathbf{x}\}$. We can define one of the outermost checker board corners as the world plane's origin and the pattern's regularity means the physical positions of every checker board corner can be calculated inside this planar coordinate system, $\{\mathbf{X}\}$. These mappings from image to world plane allow another OpenCV algorithm to estimate \mathcal{H} by minimising the residuals between real world plane positions and those generated by the projection. Following this, arbitrary image pixels can be selected, and their associated world plane positions are then estimated using equation 6.

For our 3D pinpointing method, each camera needs two world planes calibrating. These are positioned approximately coplanar to the two scintillator faces that are normal to its optical-axis, as can be seen in Figures 3a and 3b. Note that these two planes are often called the “near” and “far” planes, in reference to their relative distances from the camera. A minimum of two cameras need calibrating, and the fact our calibration planes enclose the scintillator volume is such that events emanating from that spatial region can be pinpointed. Suppose the same point-like event is imaged by two cameras and the pixel containing the event is identified in both images. The pixel can be projected onto the camera's near and far calibrated world planes; this corresponds to asking where the event would be found on those world planes if its physical position actually did lie upon them. These physical positions allow the interpolation of a line between the two planes yielding all possible positions the real event could lie along given its pixel within the captured image. Performing this interpolation for both cameras gives two lines of possible event positions; the intersection of these lines gives said event's 3D pinpointed position. The equations defining the interpolated lines are given in my Semester One report [9], where I also discuss how the directions of these lines are modified to account for refraction.

In reality, we need to define the “intersection point” of the two interpolated lines. Before a line equation can be constructed, the position from each world plane needs casting in terms of a universal coordinate system, i.e., the box's coordinate system defined in Figure 1. This introduces experimental uncertainties and thus perfect line intersection becomes unfeasible. Instead, the points from each line associated with their distance of closest approach are identified. We have deemed the mean of closest approach points, weighted by the error in their positions, as a reasonable definition for the “intersection point” between slightly skew lines.

In Semester One's implementation, since we knew how the cameras were mounted relative to the box's coordinate system, the necessary world-plane-to-box mapping was hardcoded. For our software to be compatible with future box setups, this mapping needed generalising to arbitrary camera mountings. For example, the mapping for a side-mounted camera's near calibration plane is depicted by the green arrows in Figure 3c; the red dot denotes the box's origin whereas the blue dot denotes that defined for the calibration plane. In this case, the mapping involves translation along x by both the scintillator's x -dimension and the calibration board thickness, as well as a yz translation along the calibration plane. For a top-mounted camera, the calibration plane is an xz plane instead. We call the component of this mapping along the calibration plane the “origin shift”, since it accounts for the offset in calibration board origin. Notice that if the camera's optical axis is known, the origin shift must be built from translations along the other two axes. For the camera mounting points supported by CRISP (either the side or top of the box), the origin shift is always composed of a z -offset and some non- z offset.

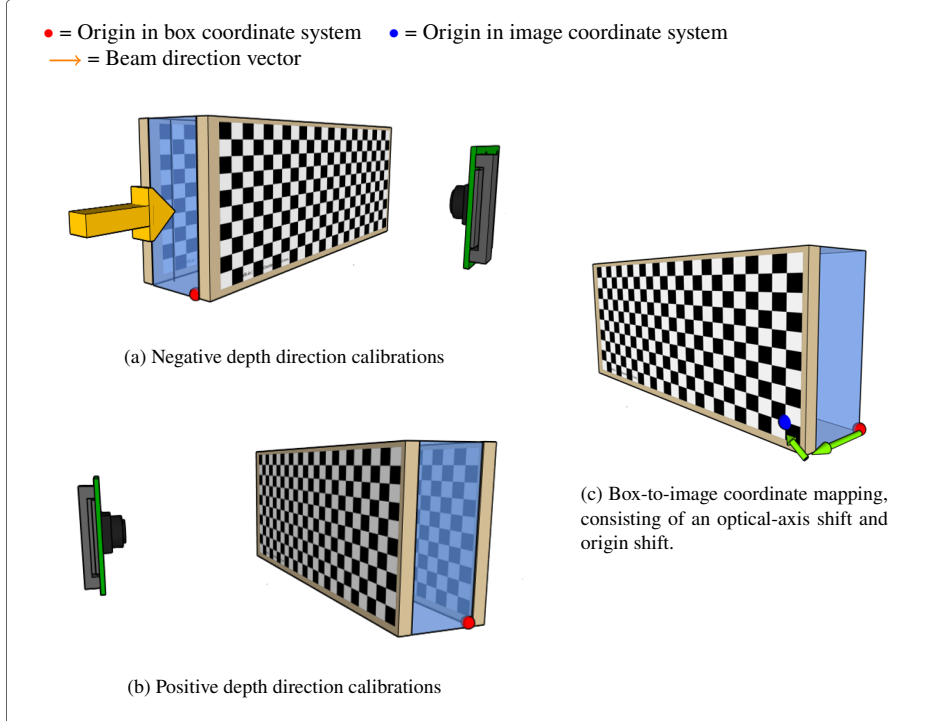


Figure 3: Homography calibrations for side-mounted cameras with (a) a negative depth direction and (b) a positive depth direction. (c) Example mapping between the calibration plane and box coordinate systems, where the figure legend labels the origins of each coordinate system.

Another subtlety to consider is how the “depth direction” of the camera influences the shift along the optical-axis when mapping between coordinate systems. The depth direction is a term we use to describe whether, for a camera with its optical-axis along the box’s i -axis, that camera has been mounted in a position with $i > 0$ (\equiv positive depth direction) or $i < 0$ (\equiv negative depth direction). Figures 3a and 3b illustrate how negative and positive depth directions impact the mapping between coordinate systems, and Table 2 summarises the corresponding shifts along the optical axis.

Table 2: Variations in the optical-axis shift of coordinate system mappings for calibrations taken with a board of thickness b . The variable d_i represents the scintillator’s dimension along the i -axis.

Camera Optical-axis	Depth Direction	Plane Position	Optical Axis Shift
i	Positive	near	$b + d_i$
i	Positive	far	b
i	Negative	near	0
i	Negative	far	d_i

5 CRISP’s GUI

In the first semester, we created a primitive interface for CRISP. However, we decided fundamental changes to camera calibration and image analysis were needed before it could be developed further. This first iteration involved using Python’s FastAPI framework for the backend logic and a frontend was constructed with simple HTML documents. Upon our return to the GUI this semester, the frontend was scrapped entirely in favour of restarting with the React framework Next.js instead. This was deemed necessary because:

1. Basic HTML offers limited native features for building intuitive, attractive graphical components.
2. If we were to build a full-stack application before our visit to the Christie Hospital, we would need to implement a framework facilitating rapid development.

5.1 CRISP Database

A key feature introduced this semester was a PostgreSQL database. When proving our methodology was viable last semester, “hard-coded” constants/file-paths were employed; a GUI needs a robust organisation of inputted data in its backend to allow our logic to generalise to the setups/calibrations created by any user. The report appendix features an Entity Relationship Diagram (ERD) that illustrates the tables comprising CRISP’s database, including the most vital columns within each table and the links that connect them.

The most essential database table is the *Camera* table, which is populated with a new record whenever a user configures a Raspberry Pi on the CRISP home page. The data stored here is needed whenever a user wants to connect to a configured Pi via Secure Shell (SSH) and each record’s primary key, its ID, allows the camera to be uniquely identified. Another vital table is the *Photos* table that stores the bytes of every image taken through CRISP. The calibration of each camera, necessary for our Bragg peak analysis, depends entirely upon the camera’s position relative to the scintillator. Therefore, if the mounted position of a camera is changed, for example, a new setup would need defining. The same applies for if the scintillator dimension’s are modified, or it is replaced by an organic scintillator of a different refractive index. As a result, the database features a *Setup* table. The user selects the cameras they wish to add to a setup, and the subsequent camera calibrations belong exclusively to that setup; i.e., a Raspberry Pi camera needs re-calibrating in a new box setup. Note the details of a camera’s calibration in a specific setup are recorded in the *CameraSetupLink* table.

When a setup is fully calibrated, the user is then available to create an experiment associated with it. Separate CRISP experiments are tracked through entries to the *Experiment* database table. Each beam run within that experiment is featured within the *Beamrun* table and the subsequent image analyses/plots are stored in the *CameraAnalysis/CameraAnalysisPlot* tables respectively.

Now that the GUI is split into three communicating services (frontend, backend and database), we needed a means of reliably synchronising their operation, and for this we implemented the containerisation tool Docker. Each service gets its own container, behaving like a virtual environment in which we can configure all the necessary code dependencies inside. Using such a tool was essential as it ensures our software will be buildable on operating systems beyond that in which it was developed.

5.2 CRISP User Experience

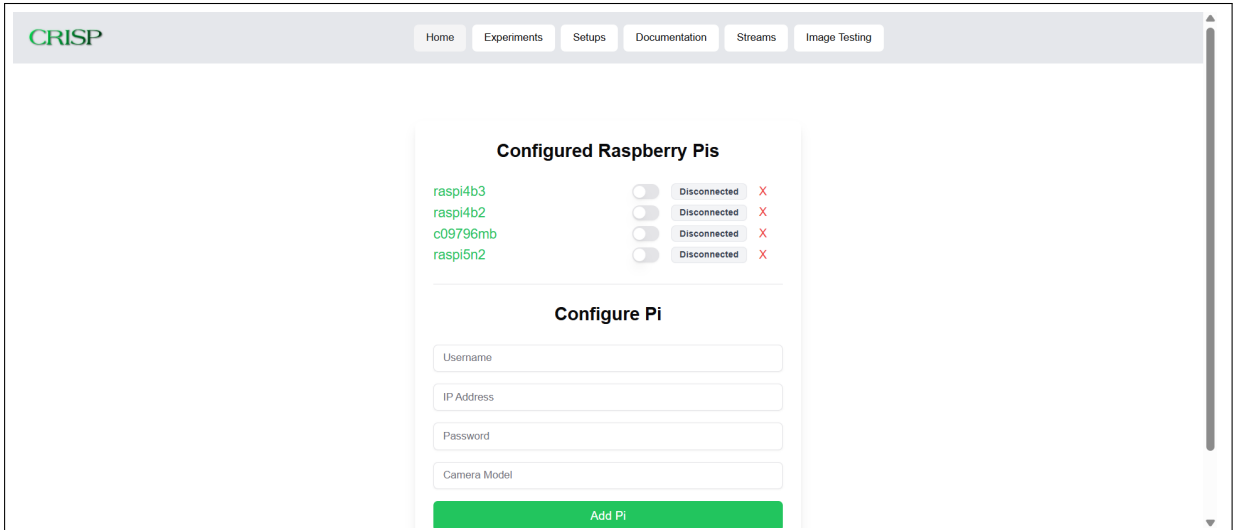


Figure 4: A screenshot of CRISP’s home page. Users can enter the credentials of new Raspberry Pi computers to configure them within CRISP. From then onwards, those Pis can be connected to using switches, each positioned next to a badge indicating the associated Pi’s connection status. Hovering over a Pi’s username (shown in green) reveals its IP address, which can be edited when clicked.

Our GUI project has aimed to abstract details of the experimental procedure in favour of a friendlier user experi-

ence. This is reflected in our software’s simple installation process - new users must only install Docker and clone CRISP’s repository. Simple Bash terminal commands like *crisp* and *close_crisp* were made to wrap the Docker commands that spin the containers up and down respectively.

After starting CRISP and navigating to port 3000 via their browser, users are greeted with its home page, as shown in Figure 4. For new users, the list of configured Raspberry Pis will be empty, so they can begin by entering the SSH credentials of each Pi. However, future Manchester users will have the option to restore CRISP’s database from a backup we have made. This contains valid camera calibrations (assuming the physical box setup is invariant), in addition to the image data we captured at The Christie’s proton beam. Once the user establishes Ethernet connections to the Pis in use, they may navigate to the Setup hub, seen within CRISP’s navigation bar.

5.2.1 Setup Pipeline



Figure 5: A screenshot of CRISP’s scintillator edge identification tool, accessed during a camera’s calibration process. The sliders move lines overlaying the image that represent the inputs of the scintillator’s edges. Hovering over the image reveals tools for panning/zooming, assisting in scintillator edge visibility and hence allowing their positions to be specified to the nearest pixel.

Creating a setup first requires the entry of the scintillator’s properties, which includes its three dimensions, refractive index, and their errors. Next, the user selects which connected cameras to include within the setup. From here, one works through the calibration process for each camera. These are initialised with the submission of input forms requesting the following settings: “lens position”, “optical axis”, “depth direction” and “image beam direction”. Lens position refers to the argument of a *rpicam* imaging command and defines the reciprocal of the camera’s focal length. Users can investigate how varying lens position influences image focus by using CRISP’s *image testing* page. The aim is to align the focal plane halfway between the near and far calibrated world planes. As discussed in Section 4, the optical-axis and depth direction need inputting for the mapping between positions on the calibrated world planes and the box’s coordinate system. The “Image beam direction” setting will be expanded upon when discussing image analysis in Section 6.

Furthermore, the input form requires the user to specify whether a distortion correction calibration should be performed or not. Last year, scintillation light images were taken using Raspberry Pi HQ cameras, which suffered from significant distortion. The four Arducam cameras used this semester had no noticeable distortion, hence we skipped this step in our calibrations. Once the initial calibration form is submitted, users must work through the next set of calibrations. If distortion correction is opted for, this must be performed first as any subsequent images will be distortion-corrected before displaying to the user.

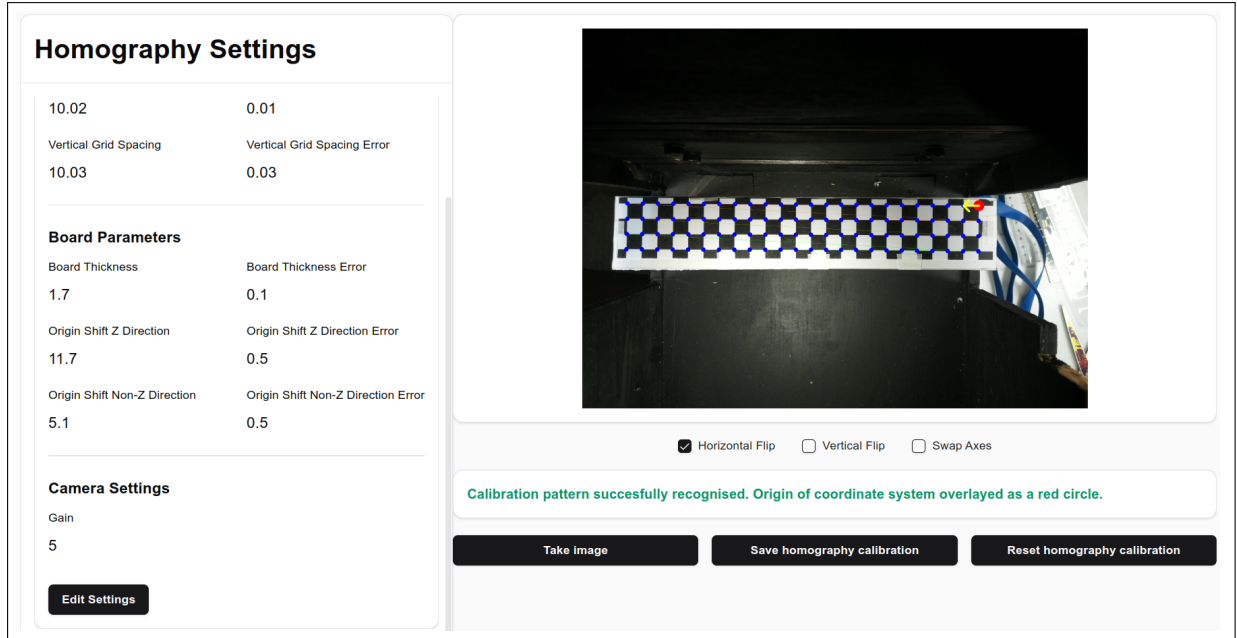


Figure 6: A screenshot of a homography creation page for the near world plane of a top-mounted camera. The left panel is used for entering the details of the calibration pattern/board and origin shift. Recognised chessboard corners are shown by blue dots, whereas the calibration pattern’s defined origin is denoted by a red dot. Before the homography calibration is saved, the user should use the checkbox transformations to move the origin until the origin shift magnitude is minimised, and the yellow arrow points in the positive z -direction.

Scintillator edge identification is one of the subsequent calibration steps, wherein the user determines what lines of pixels within that camera’s images contain the scintillator’s edges. This step is crucial to our scintillation light analysis; we should only analyse the image region we expect to see scintillation light inside, i.e. the scintillator interior. Figure 5 is a snapshot of the GUI tool for inputting the scintillator edges, in which the user moves the coloured lines until they overlay their corresponding scintillator edge.

The camera’s final two calibration steps are the construction of its far and near homographies. An example homography creation page is given in Figure 6. Here, the user enters the calibration pattern’s features. For example, the dimensions of the grid spanned by the chessboard corners is needed for OpenCV to identify all the corners. These identified corners are overlayed with blue dots on the image returned to the user. They also input the millimetre spacing between these corners in either direction, alongside their errors, measurable with digital calipers. Another crucial input is the origin shift and calibration board thickness, necessary for casting points on the plane into positions in the box’s coordinate system. The uncertainty in these shifts needs entering, also measured with calipers. Three checkboxes called “horizontal flip”, “vertical flip” and “swap axes” are used to specify transformations of the calibration pattern’s origin, represented by an overlaid red dot. The user must move this origin such that the origin shift magnitude is minimised, ensuring the yellow arrow points in the positive z -direction. This is sufficient for our backend logic to correctly interpret positions on the plane calculated through the homography.

5.2.2 Experimental Pipeline

When starting an experiment, users first select the fully calibrated setup they will be using. After this, they have the ability to start adding beam runs, with a distinction made between “test” and “real” runs. In both cases, the creation of a beam run requires the input of a beam energy (MeV) and beam current (nA).

Test runs are necessary because the scintillation light’s intensity is a function of both beam energy and current. The pixel brightness values within 8-bit images saturate at 255; we obviously wish to avoid loss of brightness data from saturation. That being said, if the image brightness is too low, the fine details of the light distribution is lost by the more pronounced quantisation of brightness. Optimum camera settings would maximise the image brightness whilst maintaining zero saturation. The scale of pixel intensities, for images of constant frame-

rate/exposure time, can be varied through the camera's analogue gain. Therefore, when establishing a test run, users enter a frame rate, maximum gain, minimum gain, and gain increment for each camera. Upon activation of the proton beam, the test run can be started and images are taken that scan the inputted gain windows. At the end of the test run, the interface signifies the optimal gain for each camera. The user is also available to view the individual colour channels of each image, with an image overlay showing the location of saturated pixels (if any).

A real run should only be performed after a test run at the same beam energy/current. If optimal settings were determined in this test run, they are the automatic settings for the real run, although the user is able to modify them if they see fit. For each camera, the user specifies the number of images to be taken, in addition to whether the “raw” images should also be saved onto the Raspberry Pis. The latter are DNG files storing the raw captures of the camera sensor. Upon the completion of a real beam run, the user is routed to a page on which they can perform the image analyses for each camera, working towards the determination of Bragg peak depth and mean range for that particular beam energy. Prior to analysing images from a camera, the user must input a colour channel to be analysed (Red, Green, Blue, Grey). Our analyses always use the blue channel since this aligns with our scintillator's emission wavelength.

The Python script created to control each Raspberry Pi's video capture allows for the format and bit depth of images to be set. Originally, we wanted to use a lossless compression format like PNG with a high bit depth to reduce compression artefacts and the effects of quantising scintillation light brightness. Despite this, we settled for traditional JPEG images with 8-bit depth. This decision reflected the fact that the large memory size of each image would have made their transfer over Ethernet impractical. The large memory size of raw images is why they too do not get transferred to CRISP's database.

6 Revised Image Analysis

The analysis procedure devised last semester was largely successful, and thus its core details remain unchanged. Nonetheless, one class of improvements focused on automating more sophisticated aspects of the analysis, generalising the process to future box setups. Another class of improvements addressed the quality of our fits and the treatment of uncertainties.

6.1 Addressing Noise in Pixel Intensities

During a real run, suppose a user requests a given camera takes N images. The scintillation light distribution should be approximately stationary soon after the proton beam's incidence to the scintillator. Light fluctuations arise due to proton range-straggling, as well as variations in the scintillator's background brightness level as generated by total internal reflection. To reduce the impact of such fluctuations, the N images are combined in the user-selected colour channel to produce a single averaged image.

Raspberry Pi cameras contain CMOS sensors which can introduce both dark current and read noise to images. Dark current arises if electrons within the sensor are thermally excited, resulting in a false light signal. For our low exposure times, and given that we average over many images, such random fluctuations contribute negligibly. Read noise arises during the analogue-to-digital conversion of the current generated by incident light into its corresponding pixel brightness. This can be partly systematic and hence would not be diminished by averaging across multiple images. We took dark frames to investigate the potential impact of read noise, but found it to be negligible in our case relative to the general uncertainty in the scintillator's background brightness level. Whilst background brightness dominates the uncertainty in the dimmer regions of the scintillator, photon shot noise is dominant in the brighter regions. With each pixel behaving like a bin of Poisson distributed photon counts, the error on pixel brightnesses in the averaged image, $\Delta\bar{B}$, is calculated using,

$$\Delta\bar{B} = \sqrt{\frac{\bar{B}}{N}}, \quad (7)$$

where \bar{B} is the pixel's average brightness value. Given the difficulty of quantifying background brightness error, it benefits us to analyse pixels in which photon shot noise dominates. Moreover, a significant source of systematic error are blemishes on the faces of the scintillator, which develop as the scintillator ages. They absorb light and thus lead to anomalous drops in the observed scintillation light intensity.

Note that how a camera is mounted inside the box determines the beam direction seen within its images; to make the averaged image consistent with the analysis that follows, it may first need rotating by a multiple of 90° to make the beam be seen entering from the left. Note the beam direction within unprocessed image is specified during the camera's calibration.

6.2 Proton Beam Edge Detection

Ultimately, we fit to the observed scintillation light distribution. Therefore, we must restrict the analysis to some sub-region of the averaged image which encloses the emitted scintillation light. The size/location of this region is constructed using edge detection techniques. Of course, the “edge” of a light distribution is somewhat arbitrary - that’s why binary thresholding is first applied. If the maximum pixel intensity within the image is I_{\max} , all pixel brightnesses B that satisfy $B \geq fI_{\max}$ will be categorised as part of the beam, where f is defined as the threshold fraction. Higher f values would exclude more of the scintillation light from the analysis. A phenomenological investigation of possible f values suggested that $f = 0.2$ was an appropriate choice. This was because, for images with correctly optimised analogue gains, this f leaves the majority of the light distribution (where photon shot noise dominates) but thresholds out its noisy tails.

Next, to ensure the edges of the thresholded beam are not significantly fractured, a morphological closing operation is applied. Then OpenCV’s “findContours” algorithm is employed to pick out points along the beam contour, but this also detects contours around anomalous bright spots in the thresholded image. These anomalies are due to scratches on the scintillator that strongly reflect light. They must be filtered out if the region-of-interest determined for our analysis is going to be useful. This filtering is achieved through the use of contour perimeters; below a certain perimeter, we define the contour as likely arising from a scintillator blemish, rather than edge detection around scintillation light.

Once all valid beam contours are identified, the extremes of horizontal and vertical pixel coordinates are extracted to define a rectangular region-of-interest (ROI) that bounds the beam. One final check is to search for ultra-low intensity pixels within the ROI. The scintillator has a background brightness level, therefore finding such intensities would imply some of the ROI is outside of the scintillator, perhaps arising from a user error with the scintillator edge identification tool. If this condition is flagged, the ROI is restricted further until it fits exclusively inside the scintillator.

6.3 Scintillation Light Fitting Procedure

Once the ROI has been determined, we begin to fit to the scintillation light distribution. The goal is to use the peaks of these fits to identify the Bragg peak’s location within the image to sub-pixel precision. First, we span the ROI horizontally, extracting every column of pixels. An ordinary least-squares fit of the generalised Gaussian model in equation 5 is performed upon each column’s intensity values. Fitting with this model would be physically justified if extracting pixel columns from the image sampled scintillation light transverse to the beam axis. This holds true only if our alignment of the beam achieves perfect normal incidence upon the scintillator, and every camera is mounted so the scintillator edges are perfectly level in its images. In reality, it is more likely the beam’s centre does not travel perfectly horizontal within the image. As a result, our column-wise sampling of pixel intensities would actually generate skewed Gaussians. If we assume that the fitted centres of these skewed Gaussians are nonetheless accurate, we can work towards a correction to the beam’s angle within the image.

We approach this correction by tracking how the fitted beam centre (a vertical pixel coordinate component) varies as we horizontally span the ROI. The theory behind multi-Coulomb scattering (Moliere theory), when applied to heavy charged particles, means the path of the beam’s centre should follow an approximate straight line. Thus, we are justified in fitting a linear model to the beam centre as a function of horizontal image coordinate. That being said, towards the end of the beam, hard scatters due to nuclear interactions result in the fitted beam centre moving more erratically within the image. This behaviour, seen at the deeper penetration depths, does not render the linear model invalid, however it does mean that the noisier region needs excluding from the linear fit. To automate the segmentation of linear/non-linear beam centre dynamics, change-point detection was implemented with the Ruptures Python library [11]. An ordinary least squares fit was performed last semester, accounting for the standard deviation in the fitted Gaussian centres. The newer fitting procedure employs orthogonal distance regression, acknowledging the quantisation noise present after pixelating the scintillation light. For a pixel of width 1, assuming the uniform distribution of incident light within the sensor region associated with the pixel, the error

in the intensity's horizontal image coordinate is given by $\frac{1}{\sqrt{12}}$. The gradient, m , of the fitted line represents the change in vertical image coordinate after changing the horizontal image coordinate; therefore, $m = \tan \alpha$, where α is the beam's angle within the image.

Using this beam angle, OpenCV's “warpAffine” method allows the pixel intensities within the image to be rotated such that the beam becomes horizontal. OpenCV's implementation of Lanczos interpolation is used to minimise the error introduced to intensities. Next, edge detection around the beam and Gaussian fitting across the ROI is repeated, since we can now fit transverse to the beam axis more confidently.

By summing the intensity of all pixels constituting a pixel column, one calculates the total intensity reaching the camera sensor from that specific depth into the scintillator. This is proportional to the linear energy transfer from the proton beam to the scintillator at that depth. Therefore, plotting the total intensities across all horizontal image coordinates in the ROI yields a distribution proportional to the proton Bragg curve. The error on total intensity of a pixel column is found by quadrature error propagation, and the horizontal image coordinate error is $\frac{1}{\sqrt{12}}$ again due to quantisation noise. An orthogonal distance regression is performed between this light distribution and the Bortfeld model, with the latter function sourced from the Python library Pybragg [12]. The fitted Bortfeld's peak is used to infer the horizontal component of the Bragg peak's pixel, with the error in peak location calculated using the multivariate delta method, explained in Section 6.6. Since this horizontal position will be of sub-pixel precision, it is necessarily rounded to the nearest pixel to map it to an associated Gaussian. The fitted beam centre of that Gaussian gives the vertical component of the Bragg peak's pixel, and thus we obtain the complete Bragg peak pixel, quoted to sub-pixel precision. Finally, the rotations applied to correct for the beam's angle, and to make the beam enter the image from the left, must be undone to recover the Bragg peak's pixel location within an unprocessed image taken by the camera.

6.4 Bragg Peak Depth Determination

Once two or more cameras have had their Bragg peak pixels identified, a button for 3D pinpointing Bragg peak positions appears within the GUI (implementing the method outlined in Section 4). As stated then, each 3D pinpointing of an event requires two cameras, since the pinpointed position corresponds to an intersection of two lines, and one line is interpolated per camera perspective of the event. Given that we are imaging with four cameras, two independent applications of the pinpointing method can be performed, and a weighted mean Bragg peak position calculated from them. We opted for only two pinpointing calculations, rather than employing all 6 possible camera combinations, to prevent the Bragg peak positions entering into the weighted mean calculation being somewhat correlated.

Using the 3D position of the Bragg peak, and the beam angles seen from the perspectives of top-mounted and side-mounted cameras, a line equation for the beam centroid's through the scintillator can be constructed. This line can then be extrapolated back from the Bragg peak onto the $z = 0$ plane; this corresponds to the beam's incident position on the anterior face of the scintillator. With this incident position, the Euclidean distance between it and the Bragg peak position gives the penetration depth associated with the Bragg peak.

6.5 Mean Range Determination

After the Bragg peak depth has been determined, each camera can have a mean range analysis performed. These require the camera's beam-axis scintillation light distribution to be cast from pixel units into physical ones. Fitting Gaussian centres when spanning the ROI tracks which pixels contain the beam's centroid across the image. In Section 6.4, we discussed the construction of this beam centroid's path through space. Therefore, if we interpolate the line of possible positions associated with each beam centroid pixel, this can be pinpointed with the beam centroid's path to compute a 3D position associated with each. Using the beam's incident position on the scintillator, each 3D position is then cast into a penetration depth. Plotting penetration depth against total scintillation light intensity at said depth produces a Bragg curve in physical units. A Bortfeld function can then be fitted with an orthogonal distance regression, and the mean range is determined by finding where the fitted Bortfeld falls to half its maximum intensity beyond the Bragg peak. The error on this range is calculated through the multivariate delta method.

6.6 Multivariate Delta Method

After fitting a d parameter model to data, the fit parameters can be gathered in a d -dimensional vector, \mathbf{p} . The fit is accompanied by a $d \times d$ covariance matrix, C . The j^{th} fit parameter has a standard deviation of $\sqrt{C_{jj}}$, but suppose we want to find the uncertainty in a quantity, $f(\mathbf{p})$, which is not an explicit fit parameter but is a function of the fit parameters nonetheless. This uncertainty can be calculated through the multivariate version of the delta method:

$$\Delta f(\mathbf{p}) = [\nabla_{\mathbf{p}} f(\mathbf{p})]^\top \cdot C \cdot \nabla_{\mathbf{p}} f(\mathbf{p}). \quad (8)$$

This method is used when we require the error in the Bortfeld peak's position or the mean range, during which these quantities get set to $f(\mathbf{p})$ in the equation above. To implement this, one fit parameter is given small perturbations above and below its nominal value while all other parameters are held constant; then, the partial gradient with respect to that fit parameter is computed through the central finite difference method. Repeating the process for all d fit parameters allows $\nabla_{\mathbf{p}} f(\mathbf{p})$ to be constructed.

7 Data Acquisition at The Christie



Figure 7: (a) shows the Christie's beam nozzle behind our CRISP box setup. (b) captures the water beam stop beyond the box. These images were taken by my project partner, Robin de Freitas.

For live analysis to be performed with CRISP at The Christie, a box setup, complete with all camera calibrations, needed creating before our arrival. The origin shifts of calibration patterns were measured to within 0.5 mm of error, and the calibration board's thickness had a 0.1 mm error. Our experiments were performed using Beamline A in the hospital's Stoller Research Room [3], with the final setup of our apparatus pictured in Figure 7. The beamline's nozzle, seen behind the box in Figure 7a, is located at the end of an array of quadrupole magnets used to focus the beam. Figure 7b shows a water beam stop beyond the box that brings protons passing through/past our setup to rest.

The process of setting up the box began with aligning the beam's path to be normally incident upon the scintillator. We clamped the box to a scissor lift placed on a table in front of the beam nozzle, allowing the box to be raised into the beam's path. The beamline features a green LAP laser system [3], visible in Figure 7b, intended to assist such alignments. Note that a pencil line is drawn on the side of our box to mark the vertical centreline of the scintillator inside. Therefore, after raising the box, the tracing of an alignment laser along that pencil line helped indicate there was no noticeable beam angle in the yz plane. Next, a pencil outline of the scintillator was drawn on the base of the box. Since another laser follows the path to be taken by the proton beam centroid, that laser's position was measured relative to the scintillator outline at various points along it, checking the centroid position remained constant and hence confirming there was no noticeable xz beam angle.

After setting up and testing the Raspberry Pi Ethernet networking, the scintillator was polished and any unnecessary gaps into the box were sealed using tape, reducing the risk of external light leaking inside. Following this we were given a radiation protection briefing by Professor Michael Taylor. This involved collecting Thermoluminescent Dosemeter (TLD) badges [13] to wear so that we could be later notified if we were exposed to a significant dose of radiation. A critical safety measure was the use of a traffic light system in the beam's control room for clearly

conveying the beam's status. After the beam's operation, and enough time had passed for sufficient activated air to be evacuated from the room, we would be allowed to return to our apparatus. However, we would bring radiation detectors to check the activity of our equipment before interacting with it.

We had discussed what beam energies we would be using with a PhD student within the group, Mosst Tasnim Binte Shawkat, who was taking measurements simultaneously with us. We settled on the following five in order to test our analysis across a wide energy range: $\{70, 110, 130, 150, 170\}$ MeV. Before each beam run, these energies needed requesting from the cyclotron's operator by Professor Michael Taylor. The beam was kept active for only two minutes at a time, which was enough to capture 60 JPEG images of the beam without saving the raw sensor data, or 25 JPEGs whilst saving raw sensor data. Given our interest in demonstrating successful image analysis through CRISP, we opted for the greater number of JPEG images to ensure each averaged image of the beam was as accurate as possible.

On the whole, CRISP was a successful system for imaging the scintillator, e.g., the GUI made creating test and real beam runs simple. Despite this, some issues arose during data acquisition. One such issue was that one Raspberry Pi computer, associated with the FS camera in Figure 1, was particularly temperamental during imaging. Sometimes this camera would successfully take images and return them to CRISP, but often imaging would unexpectedly halt. Initially, it seemed to be related to the beam's operation; this Pi was mounted the closest to the beam's trajectory, so maybe stray protons were interfering with the computer. That being said, issues with Ethernet connections had been recently raised in the Stoller Research Room, and so its possible that this alone explains the FS camera's intermittent failures.

An unanticipated difficulty was the selection of appropriate test-run frame rates as a function of beam energy/current. We believed 20 FPS could be selected across all beam runs, with the gain optimisation algorithm selecting the optimal analogue gain subject to that exposure time. In reality, this set an upper bound on possible pixel intensity, occurring at the maximum analogue gain of 16. Therefore, for the lower beam currents in which the scintillator's absorbed dose was lower, the optimised gain would be 16 and yet the scintillation light would still be too faint. This meant we had to repeat test beam runs with lower frame rates until a test image with optimally bright scintillation light was taken. For this reason, the gain optimisation algorithm should be amended to span across various frame rates, as well as gains, in its search for the settings with optimal pixel intensities.

8 Results



Figure 8: FS camera's region-of-interest inside scintillator at 150 MeV. This is where pixel intensities will be analysed.

As mentioned in Section 7, we took real beam runs at five beam energies. In this section, the key plots for only one energy, 150 MeV, are presented, although the Bragg peak depths determined for all energies will be provided. Note that these plots can be generated for each camera used within a beam run. Only those for the FS camera (refer to Figure 1) are shown here. The region-of-interest (ROI) for image analysis, achieved using edge detection techniques, is displayed in Figure 8.

8.1 150 MeV Beam Angle Extraction

Figure 9 is the result of plotting the fitted Gaussian centre as a function of horizontal image coordinate. Across the ≈ 900 pixels of this plot, the vertical coordinate of the beam centroid falls monotonically by roughly 20 pixels; visually, the motivation for fitting a linear model is clear. The residuals between experimental and fitted beam centre shows that the fit is always correct to within a pixel. The reduced χ^2 statistic of 4.88 indicates the uncertainty on fitted beam centres is likely too small. The fitted beam angle seen within the image is $-1.078 \pm 0.002^\circ$, wherein underestimated beam centre errors have lead to an underestimated beam angle error. Nonetheless, the clear presence of an observed beam angle, whether due to the camera's mounted orientation or misalignment of the beam, suggests correcting for an angle is appropriate. Moreover, this step is key for a generally applicable image analysis, as future CRISP users may see more pronounced beam angles in their images. It is possible that for sufficiently small angles, the error introduced interpolating intensities during the image's rotation outweighs the benefit of beam angle correction – something which could be investigated further.

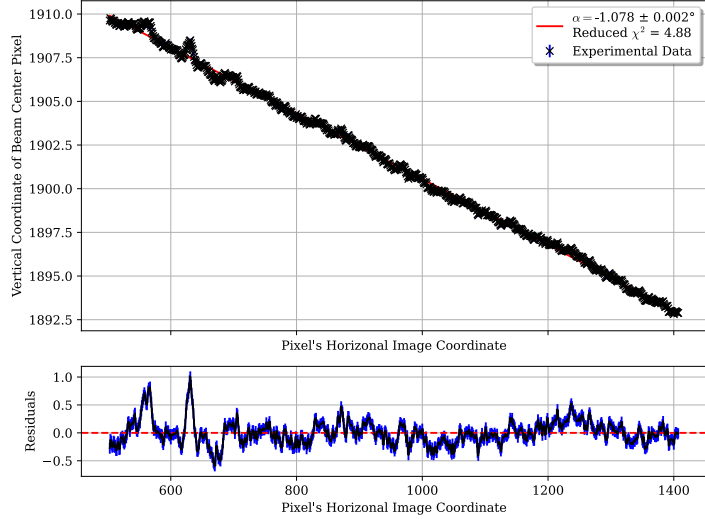


Figure 9: Angle extraction plot for FS Camera at 150 MeV beam energy, in which the error bars are too small to be seen. The reduced χ^2 is 4.88, and the fitted beam angle is $-1.078 \pm 0.002^\circ$.

8.2 150 MeV Gaussian Fits

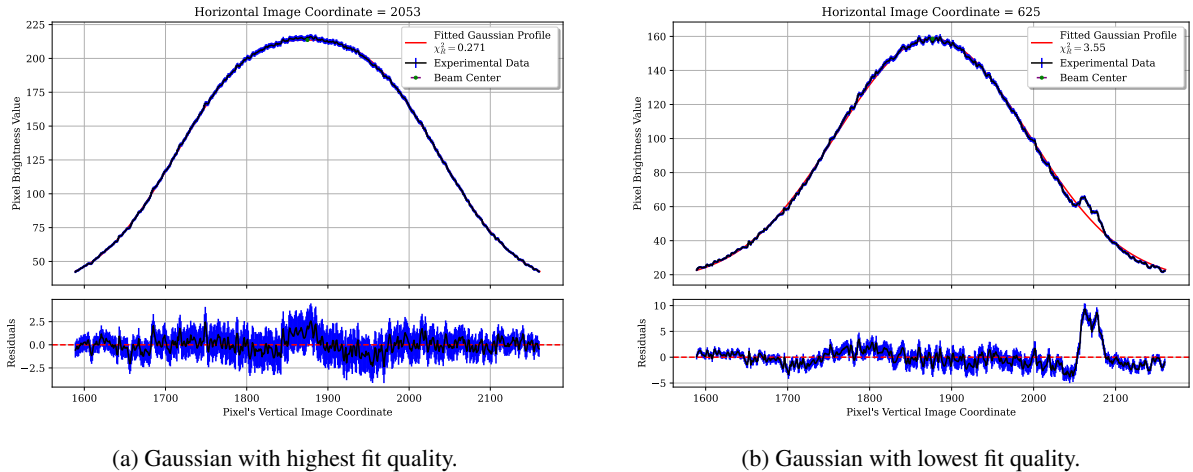


Figure 10: Generalised Gaussian fits, for FS camera at 150 MeV beam energy, with the highest and lowest fit qualities. These have reduced χ^2 statistics of 0.271 and 3.55 respectively. Blue error bars are attached.

After correcting for the beam's angle, Gaussian fitting is performed transverse to the beam axis; the fits with highest and lowest reduced χ^2 statistics are presented in Figure 10. The highest fit quality, shown in Figure 10a, has a reduced χ^2 of 0.271. This can normally signify an overestimate of uncertainty, but the only uncertainty included here arises from the photon shot noise in pixel intensities. Since the other sources of intensity error are unaccounted for, overestimated errors are unlikely. Instead, perhaps the generalised Gaussian model (refer to Equation 5) leads to some over-fitting. The reason this model is still used is that, when using a traditional Gaussian model, the fit quality is worst around the Bragg peak, i.e. the region in which hard proton scatters exacerbate beam broadening, and the reduced χ^2 statistics reach ~ 15 . Given that accurate fits are essential around the Bragg peak, to accurately 3D pinpoint its position inside the scintillator, the generalised Gaussian model is favoured. Within Figure 10b, the worst fitting Gaussian is shown, with a reduced χ^2 of 3.55. An obvious anomaly in intensity is present. For other camera analyses, the worst fitting Gaussian can have anomalous drops in intensity. When cross-referencing patches of anomalous intensity with a camera's scintillator images, they correspond to scratches/blemishes on the face of the scintillator that diffusely reflect/absorb scintillation light. These introduce systematic error which is not easily accounted for, especially since less visible imperfections could tarnish the entire scintillator. Maybe such imperfections subtly bias the fitted Gaussians, which could explain why the Gaussian centres in Figure 9 have underestimated errors.

8.3 150 MeV Bortfeld Fits

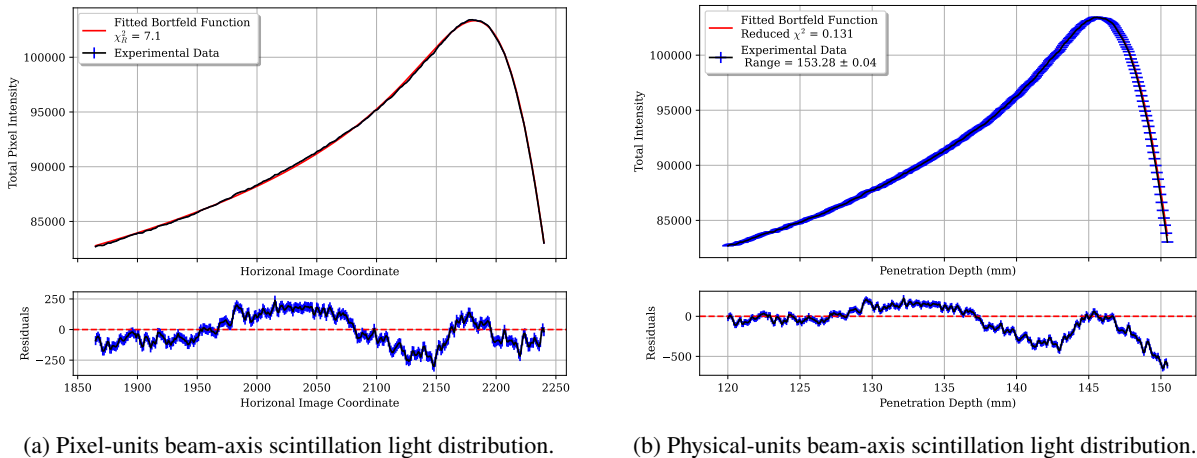


Figure 11: Bortfelds fitted to beam-axis scintillation light distribution im terms of (a) pixel-based units and (b) physical units.

Within Figure 11, the fitted Bortfeld functions can be seen. Figure 11a shows the Bortfeld fitted to the scintillation light with pixel-based units for depth along the z -axis. This fit has a reduced χ^2 of 7.1, with the residual between the best-fit Bortfeld and intensity data being notable. Note the total intensity at a given horizontal image coordinate must be constructed from a column of pixels which vertically spans the full scintillator, not just the ROI determined for the beam. As a result, intensity values in which the scintillator's background brightness dominates are included, however these pixels have their intensity errors estimated only as photon shot noise. In addition to this, artefacts on the scintillator faces will systematically modify the observed scintillation light intensity. For example, for these pixels of 8-bit depth, a total intensity residual of ≈ -255 could be due to an absorbing blemish with the angular size of a single pixel. Despite this, the Bortfeld fits the distribution visibly well, hence we can expect its peak position to give an accurate horizontal component to the Bragg peak pixel.

Figure 11b shows a fit to the same distribution, but with the abscissa converted to beam-axis penetration depth in millimetres. The intensity values are unchanged, thus the same explanation for intensity residuals holds. The reduced χ^2 is now 0.131; this being smaller corresponds to the larger horizontal uncertainty associated with each point. Each position along the beam centroid has been 3D pinpointed, which introduces the errors in our camera calibrations. The experimental and fitted dose curves show minimal horizontal residuals relative to the horizontal error bar sizes, indicating the pinpointed depths have overestimated error. We know a Bortfeld fit is appropriate for the beam-axis scintillation light distribution; therefore, if we naively expect a near-perfect fit, the approximate factor by which horizontal error bars must scale is $\sqrt{\chi_R^2}$, wherein χ_R^2 is the reduced χ^2 . This suggests the error

bars are roughly 3 times too large.

One explanation for this is a suspected misuse of error propagation techniques. Let the lines interpolated for the two cameras during the 3D pinpointing method have the parameterising points $\{\mathbf{p}_1, \mathbf{p}_2\}$ and directional vectors $\{\mathbf{d}_1, \mathbf{d}_2\}$. The closest point on line 1 to line 2, \mathbf{q}_1 , is given by,

$$\mathbf{q}_1 = \mathbf{p}_1 + \frac{(\mathbf{p}_2 - \mathbf{p}_1) \cdot (\mathbf{d}_2 \times \mathbf{d}_1 \times \mathbf{d}_2)}{\mathbf{d}_1 \cdot (\mathbf{d}_2 \times \mathbf{d}_1 \times \mathbf{d}_2)} \mathbf{d}_1 \quad (9)$$

When combining experimental errors to get the error on \mathbf{q}_1 , the errors on sub-factors were computed first, before those factors were propagated together. Assuming zero covariance, the variance on a quantity $y(\mathbf{x}_i)$, dependent on variables of uncertainty Δx_i , is calculated as,

$$\sigma_y^2 = \sum_i \left(\frac{\partial y}{\partial x_i} \Delta x_i \right)^2. \quad (10)$$

Crucially, this approach is valid if the inputted uncertainties are Gaussian distributed and statistically independent, but splitting the calculation into sub-factors that share variables introduces correlation. This inflates the error on the derived quantity. Amending this oversight could be pivotal to taming the overestimation of errors on pinpointed depths.

8.4 Bragg Peak Depths

Our experimental depths are compared to those determined within Monte-Carlo simulations of our CRISP box setup. The software TOPAS [14] was used, a Geant4-based tool which specialises in radiotherapy applications, e.g., producing dose distributions inside a medium. Note the key material parameters influencing proton stopping power are the scintillator's chemical composition and mass density. For a given simulated beam energy, E_B , 10,000 protons are made to traverse 82 cm of air (modelling the gap between the beam's nozzle and the scintillator). Following this, they traverse 5 mm of LDPE, representing a bin bag which was taped to the beam's entrance to close the box from external light. Only after traversing these materials do the protons enter the PVT scintillator. The scintillator is partitioned into cubic bins such that the LET deposited into each can be recorded. Summing the LET deposited into all bins of a given beam-axis depth produces a Bragg curve dose distribution along said axis; a Bortfeld function can then be fitted, with the fit's peak corresponding to the simulated Bragg peak depth at E_B .

The Bragg peak depths determined through our experimental analysis are given in Table 3, alongside two sets of simulated Bragg peak depths. One set was generated under the assumption that The Christie's proton transport system can deliver the proton beam into the Stoller Research Room at the nominal energy established by their Energy Selection System (ESS). Discussions with Professor Michael Taylor indicated that the energies of protons exiting the nozzle are actually attenuated relative to the ESS energy, resulting from imperfect vacuums through which the beam is transported. The uncertainty in beam nozzle energy is energy-dependent, but is said to range between 0.7-1.7 MeV. In response to this, a second set of simulated depths were determined, with energies 1.7 MeV below the ESS energy; this yields a lower bound on the expected Bragg peak depth. Each simulated depth is quoted with asymmetric errors, stemming from the 0.03 g cm^{-3} error in our scintillator's 1.04 g cm^{-3} density. Bethe-Bloch stopping power is proportional to the density of the medium being traversed, hence the error lowering the Bragg peak's depth is associated with a 1.07 g cm^{-3} scintillator simulation.

The residuals between these depths are illustrated within Figure 12. The experimental and simulated Bragg peak depths have had their simulated depth at the ESS energy, D_{ESS} , subtracted to emphasise the deviation between the experimental and simulated values. Experiment and theory are consistent at all energies, however this unsurprising given the significant errors introduced to simulated depths by uncertainty in the scintillator's density. The 3% error in the scintillator's mass is a consequence of the measurement being made using an analogue weighing scale. Unfortunately, we have only recently appreciated how impactful the error on density is to our simulated depths, otherwise the mass measurement could have been repeated with a digital weighing scale. Additionally, instead of always calculating lower bounds on Bragg peak depths by imposing 1.7 MeV attenuation, these bounds would be more useful if it followed the true energy-dependence of attenuation seen at The Christie's beamline.

8.5 Experimental Mean Ranges

The mean ranges determined through our image analyses are given in Table 3. A range analysis can be performed for each camera, but the quoted ranges were all obtained from the NS camera. However, its important to note that

Table 3: Experimental (EXP) and simulated (SIM) Bragg peak depths as a function of beam energy. The simulated depths are at the ESS-quoted beam energy and that attenuated by 1.7 MeV. The asymmetric errors on simulated depths arise when varying the scintillator’s density by its measured uncertainty. Experimentally determined mean ranges are also given.

Beam Energy	EXP Mean Range [MeV]	EXP BP Depth [mm]	SIM BP Depth [mm]	SIM Attenuated BP Depth [mm]
70	37.18 ± 0.01	33.43 ± 0.59	$33.15^{+0.94}_{-0.99}$	$31.43^{+0.91}_{-0.91}$
110	87.82 ± 0.03	82.95 ± 0.29	$81.48^{+2.44}_{-2.27}$	$79.19^{+2.23}_{-2.26}$
130	118.13 ± 0.03	112.64 ± 0.30	$111.44^{+3.34}_{-3.05}$	$108.76^{+3.28}_{-2.97}$
150	152.77 ± 0.03	145.52 ± 0.29	$145.08^{+4.18}_{-3.82}$	$142.14^{+4.02}_{-4.03}$
170	190.96 ± 0.03	181.95 ± 0.58	$181.83^{+5.55}_{-5.29}$	$178.49^{+5.41}_{-5.06}$

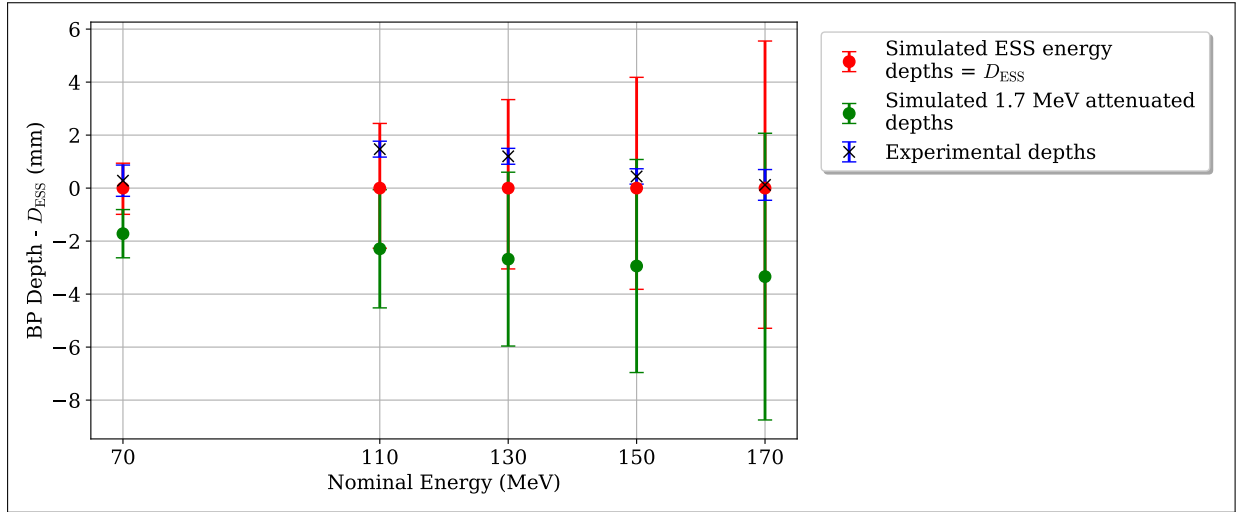


Figure 12: A plot of the residuals between experimental Bragg peak depths and the depths from simulations at the nominal ESS beam energy. The green data points show the residuals between the simulated depths at the nominal ESS energy and the simulated depths with a beam attenuated by 1.7 MeV. All experimental Bragg peak depths are consistent with the simulation at nominal ESS energy.

two range analyses for different cameras from the same beam run can show inconsistent mean ranges. The residual can be up to 2 mm, which is 2 orders of magnitude above the quoted range errors. Since the range calculation is the culmination of all analysis steps thus far, this inconsistency implies some flaw in the methodology. Referring back to Section 6.6, the multivariate delta method will underestimate the mean range error if the covariance matrix is too small, arising from an overly confident fit. We see that this is the case when fitting Bortfelds to the beam-axis scintillation light distribution because of the overestimated error on depths determined by our 3D pinpointing method. This reinforces the need to revisit error propagation in the 3D pinpointing method, since the true precision of our mean range measurements remains inconclusive.

We have not obtained mean ranges from our TOPAS simulations due to a lack of knowledge surrounding the proton beam’s energy distribution. Protons of different energies will peak in their LET at different depths, hence a distribution around the beam’s nominal energy smears the Bragg peak to be of finite width. All protons leave the cyclotron with the same energy, associated with the speed at which they are extracted, however they are reduced to clinical energies by the ESS. This system consists of a carbon stepped degrader, placed into the path of the beam [3] to attenuate them on average by,

$$\Delta E = S\Delta t, \quad (11)$$

where S is the proton stopping power and Δt the thickness of the step. The statistical nature of proton-electron interactions, and the variable proton path-length through the carbon step due to scattering, results in a Gaussian

energy distribution, skewed towards the lower energies. Since we have no knowledge of this distribution's width, we cannot meaningfully simulate the broadening of Bragg peaks, thus simulated mean ranges would be inaccurate. One possible extension to our project would be to properly model the energy-straggling inherent within The Christie research room's beam energies, so that simulated mean ranges could be generated.

8.6 Analysis Evaluation

This semester, the significant uncertainty on simulated depths has hindered our ability to discuss the accuracy and precision of experimentally determined Bragg peak depths. That being said, the residuals between the experimental depths and those simulated at the ESS energy are within 2 mm; therefore, the method we have devised this year certainly shows its potential for identifying Bragg peak depths. Our results could be immediately refined by repeating the simulations with a more precise measurement of the scintillator's density, after having weighed it with digital scales.

As for the dominant experimental errors, I have discussed how the error on positions determined through 3D pinpointing are likely overestimated due to flaws in the error propagation procedure. The error in world plane positions determined through our homographies could be reduced further by using finer calibration patterns. This is because more feature point mappings would be known to inform OpenCV's homography matrix estimation. That being said, the origin shift added to world plane positions has two components, each of 0.5 mm error. This dominates over the homography error, hence measuring origin shifts to higher precision should be attempted. Furthermore, an inaccurate refractive index for the scintillator will shift the Bragg peak depth. Thus, a means of directly determining the refractive index of the scintillator at its emission wavelength should be explored, so that a literature PVT refractive index need not be relied on.

Finally, a possible flaw in the current analysis procedure is how the beam angle is interpreted. Correcting for beam angles seen within images is valid, however these angles are not necessarily the angles relative to the anterior face of the scintillator – an apparent angle can be seen due to how the camera was mounted inside of the box. As a result, constructing a vector for the beam's path through space with these angles can be inaccurate. In the future, the beam's path could be built from beam angles taken relative to the angle of the scintillator's edges within the images.

9 Future Work

Extensions of this project can be divided into two categories: further development of CRISP and increasing simulation sophistication. CRISP's GUI is already effective at keeping the user experience (UX) simple, however this UX could always be streamlined with the automation of additional calibration steps. For example, the optimal focus is currently determined manually for each camera. Focus optimisation could be automated with a script that takes multiple images (of different focal lengths) containing a chessboard pattern at the desired focal plane. Then, the focus setting that maximises total Laplacian variance across the image may imply its image is the sharpest. In addition to this, I described in Section 7 how the test-run system for optimising analogue gain was limited by the user-selected frame rate (a proxy for exposure time). Therefore, an updated gain optimisation algorithm should vary both image gain and frame rate.

Moreover, during data acquisition at the Christie, we had to manually back-up our data to an external hard-drive between beam runs. PostgreSQL databases allow for Write-Ahead Logging (WAL), which could be implemented by future developers such that the creation of database backups is automated.

Concerning the TOPAS simulations of our box setup, an investigation of the total internal reflection of scintillation light inside of the scintillator could motivate more advanced estimates of error on observed pixel intensities. Future simulations could also indicate how experimental effects could bias our cameras to observe the peak dose at shallower/deeper depths than the true Bragg peak depth. The observed scintillation light intensity is proportional to the absorbed dose in Equation 1, but is damped by the scintillator's efficiency. Perhaps, the effective scintillator efficiency varies with position inside it, due to the attenuation of light and ionisation quenching [15].

10 Conclusion

Overall, CRISP has fulfilled our initial objective of producing a graphical user interface for proton beam monitoring. To achieve this, we have had to devise new methods of camera calibration and image analysis which are capable of being automated in the interface’s backend. The sub-2 mm residuals between the experimentally measured and simulated Bragg peak depths show our methodology is promising. Nevertheless, the quoted precision on experimental and simulated Bragg peak depths are overestimated, particularly the simulated depths due to the large error associated with the measured scintillator density. Importantly, even if future users would prefer to implement their own calibrations and analyses, CRISP’s “Experiments” section provides an intuitive tool for configuring optimal scintillation light imaging.

References

- [1] R. R. Wilson, “Radiological Use of Fast Protons,” en, *Radiology*, vol. 47, no. 5, pp. 487–491, Nov. 1946, ISSN: 0033-8419, 1527-1315. doi: 10.1148/47.5.487. [Online]. Available: <http://pubs.rsna.org/doi/10.1148/47.5.487> (visited on 12/11/2024).
- [2] R. Mohan, “A review of proton therapy – Current status and future directions,” en, *Precision Radiation Oncology*, vol. 6, no. 2, pp. 164–176, Jun. 2022, ISSN: 2398-7324, 2398-7324. doi: 10.1002/pro6.1149. [Online]. Available: <https://onlinelibrary.wiley.com/doi/10.1002/pro6.1149> (visited on 05/08/2025).
- [3] J. D. Aylward, N Henthorn, S Manger, et al., “Characterisation of the UK high energy proton research beamline for high and ultra-high dose rate (FLASH) irradiation,” *Biomedical Physics & Engineering Express*, vol. 9, no. 5, p. 055 032, Sep. 2023, ISSN: 2057-1976. doi: 10.1088/2057-1976/acef25. [Online]. Available: <https://iopscience.iop.org/article/10.1088/2057-1976/acef25> (visited on 12/09/2024).
- [4] *Arducam IMX519 Camera Specification*, en. [Online]. Available: <https://www.arducam.com/product/imx519-autofocus-camera-module-for-raspberry-pi-arducam-b0371/> (visited on 12/05/2024).
- [5] *PDG Atomic and nuclear properties of polyvinyltoluene*. [Online]. Available: <https://pdg.lbl.gov/2014/AtomicNuclearProperties/HTML/polyvinyltoluene.html> (visited on 12/05/2024).
- [6] H. Nakamura, Y. Shirakawa, N. Sato, et al., “Optical characteristics of pure poly (vinyltoluene) for scintillation applications,” en, *Nuclear Instruments and Methods in Physics Research Section A: Accelerators, Spectrometers, Detectors and Associated Equipment*, vol. 770, pp. 131–134, Jan. 2015, ISSN: 01689002. doi: 10.1016/j.nima.2014.10.018. [Online]. Available: <https://linkinghub.elsevier.com/retrieve/pii/S0168900214011656> (visited on 12/09/2024).
- [7] B. Gottschalk, *Radiotherapy Proton Interactions in Matter*, arXiv:1804.00022 [physics], Mar. 2018. doi: 10.48550/arXiv.1804.00022. [Online]. Available: <http://arxiv.org/abs/1804.00022> (visited on 05/08/2025).
- [8] T. Bortfeld and W. Schlegel, “An analytical approximation of depth - dose distributions for therapeutic proton beams,” *Physics in Medicine and Biology*, vol. 41, no. 8, pp. 1331–1339, Aug. 1996, ISSN: 0031-9155, 1361-6560. doi: 10.1088/0031-9155/41/8/006. [Online]. Available: <https://iopscience.iop.org/article/10.1088/0031-9155/41/8/006> (visited on 12/09/2024).
- [9] L. Dean, “Developing an Automated Analysis for Proton Beam Monitoring,” 2024.
- [10] R. de Freitas, “Developing an automated system for proton beam calibration using Raspberry Pi cameras,” 2024.
- [11] C. Truong, L. Oudre, and N. Vayatis, “Selective review of offline change point detection methods,” en, *Signal Processing*, vol. 167, p. 107 299, Feb. 2020, Publisher: Elsevier BV, ISSN: 0165-1684. doi: 10.1016/j.sigpro.2019.107299. [Online]. Available: <https://linkinghub.elsevier.com/retrieve/pii/S0165168419303494> (visited on 05/01/2025).
- [12] *Pybragg Python Package*. [Online]. Available: <https://github.com/flome/pybragg> (visited on 12/06/2024).
- [13] UK Health Security Agency, *Body Thermoluminescent Dosimeter (TLD)*. [Online]. Available: https://www.ukhsa-protectionservices.org.uk/cms/assets/gfx/content/resource_2963csb887d8d5e6.pdf.

- [14] *Topas - Tool for Particle Simulation Wesbite Home Page*. [Online]. Available: <https://www.topasmc.org/home> (visited on 12/05/2024).
- [15] T. Pöschl, D. Greenwald, M. J. Losekamm, and S. Paul, “Measurement of ionization quenching in plastic scintillators,” en, *Nuclear Instruments and Methods in Physics Research Section A: Accelerators, Spectrometers, Detectors and Associated Equipment*, vol. 988, p. 164 865, Feb. 2021, issn: 01689002. doi: 10.1016/j.nima.2020.164865. [Online]. Available: <https://linkinghub.elsevier.com/retrieve/pii/S0168900220312626> (visited on 05/08/2025).

Appendix

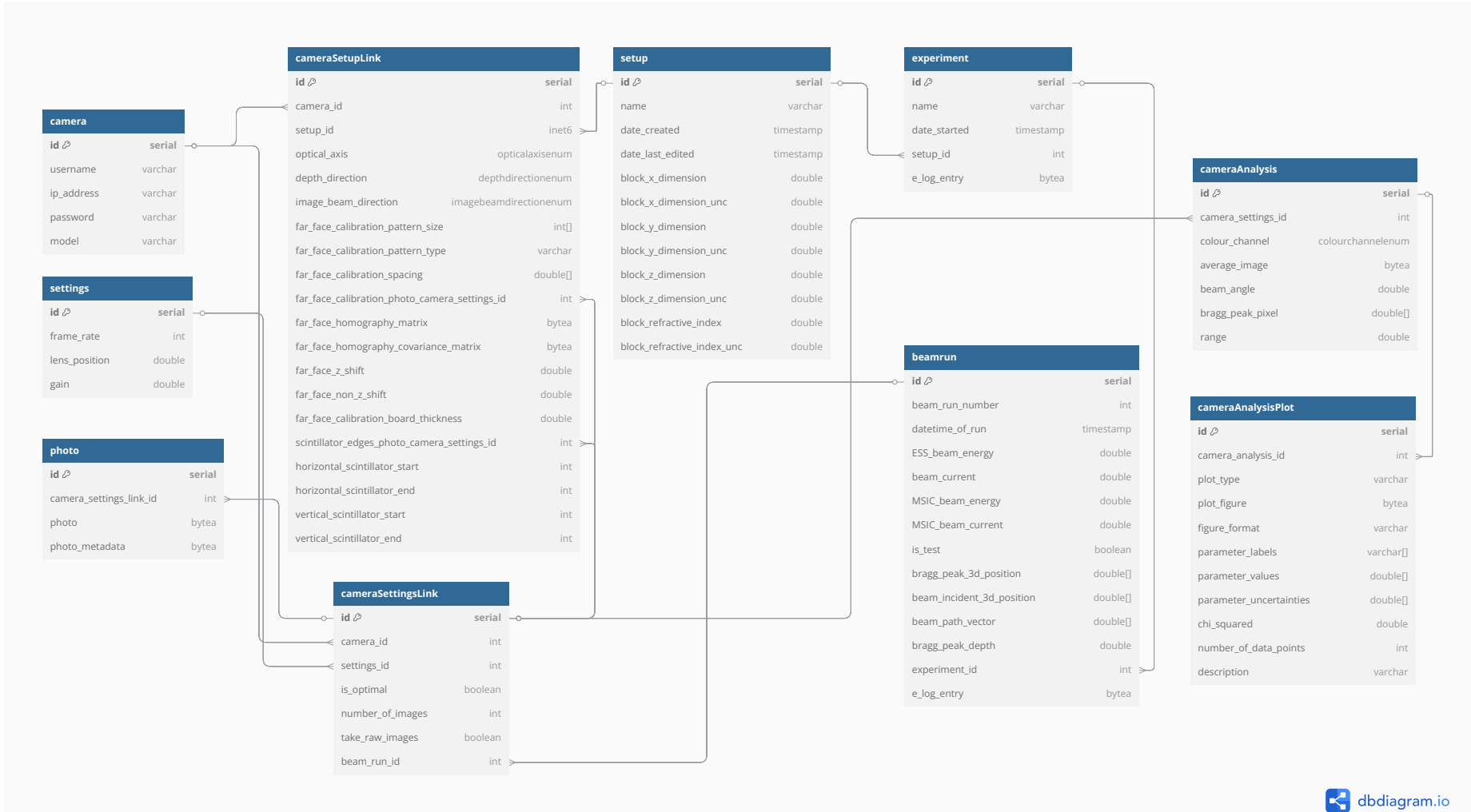


Figure 13: Entity Relationship Diagram for CRISP Database. For brevity, all table columns storing uncertainties for columns already displayed have been suppressed. Additionally, the cameraSetup table has an extra set of fields for the near world plane of the homography calibration, and the table's distortion calibration fields are also omitted.